

- Sager, W. W., 1983b. A late Eocene paleomagnetic pole for the Pacific plate, *Earth planet. Sci. Lett.*, **63**, 408–422.
- Sager, W. W., 1987. Late Eocene and Maestrichtian paleomagnetic poles for the Pacific plate: implications for the validity of seamount paleomagnetic data, *Tectonophysics*, **144**, 301–314.
- Sager, W. W. & Pringle, M. S., 1988. Mid-Cretaceous to early Tertiary apparent polar wander path of the Pacific plate, *J. geophys. Res.*, **93**, 11 753–11 771.
- Schneider, D. A., 1988. An estimate of the long-term non-dipole field from marine magnetic anomalies, *Geophys. Res. Lett.*, **15**, 1105–1108.
- Schouten, H., 1971. A fundamental analysis of magnetic anomalies over oceanic ridges, *Mar. geophys. Res.*, **1**, 111–114.
- Schouten, H. & Cande, S. C., 1976. Palaeomagnetic poles from marine magnetic anomalies, *Geophys. J. R. astr. Soc.*, **44**, 567–575.
- Schouten, H. & McCamy, K., 1972. Filtering marine magnetic anomalies, *J. geophys. Res.*, **77**, 7089–7099.
- Suarez, G. & Molnar, P., 1980. Paleomagnetic data and pelagic sediment facies and the motion of the Pacific plate relative to the spin axis since the Late Cretaceous, *J. geophys. Res.*, **85**, 5257–5280.
- Tarduno, J. A., 1990. Absolute inclination values from deep sea sediments: A reexamination of the Cretaceous Pacific record, *Geophys. Res. Lett.*, **17**, 101–104.
- van Andel, T. H., Heath, G. R. & Moore, T. C., 1975. Cenozoic history and paleoceanography of the central equatorial Pacific ocean, *Geol. Soc. Am. Mem.*, **143**, 134.
- Weissel, J. K. & Hayes, D. E., 1972. Magnetic anomalies in the southeast Indian Ocean, in *Antarctic Oceanology II: The Australian–New Zealand Sector*, Antarctic Res. Ser. 19, pp. 165–196, ed. Hayes, D. E., AGU, Washington, DC.
- Winterer, E. L., 1973. Sedimentary facies and plate tectonics of the equatorial Pacific, *AAPG*, **57**, 265–282.

## Inversion of teleseismic *S* particle motion for azimuthal anisotropy in the upper mantle: a feasibility study

V. Farra,<sup>1</sup> L. P. Vinnik,<sup>2</sup> B. Romanowicz,<sup>1</sup> G. L. Kosarev<sup>2</sup> and R. Kind<sup>3</sup>

<sup>1</sup> *Laboratoire de Sismologie, Institut de Physique du Globe de Paris, 4 Place Jussieu, F-75252 Paris cedex 05, France*

<sup>2</sup> *Institute of the physics of the Earth, Soviet Academy of Sciences, Moscow, USSR*

<sup>3</sup> *Seismologisches Zentralobservatorium, Krankenhausstraße 1–3, 8520 Erlangen, FRG*

Accepted 1991 February 28. Received 1991 February 28; in original form 1990 October 5

### SUMMARY

We have developed a technique for the inversion of teleseismic *S*-waveforms in terms of azimuthal anisotropy in the upper mantle. We test different models of the Earth upper mantle by transforming the observed horizontal components into a synthetic vertical component and comparing this with the observed vertical component. The optimum model is found by minimizing the difference between the synthetic vertical component and the observed one. Using this method, we explore the possibility of constraining the distribution of azimuthal anisotropy with depth.

We present examples of seismic observations where the data are clearly in favour of an anisotropic model. These observations can be interpreted in terms of two anisotropic layers with different directions of fast velocity axes.

**Key words:** anisotropy, mantle discontinuities, *P* precursor.

### 1 INTRODUCTION

Recent studies of *SKS* polarization indicate the presence of azimuthal anisotropy in the continental upper mantle (e.g. Kind *et al.* 1985; Silver & Chan 1988; Vinnik, Farra & Romanowicz 1989). Unfortunately the observations of *SKS* provide little information on the distribution of anisotropy with depth, which is of crucial importance for understanding the origins of this phenomenon. Some attempts to solve this problem were previously described in the literature. Seismic refraction observations on profiles crossing the same area in several directions may provide data on the magnitude of the *P*-wave anisotropy, the azimuth of the axis of fast velocity and the depth interval where the effect is observed. These techniques were applied with some success in the oceans (e.g. Hess 1964; Shimamura 1984; Shearer & Orcutt 1985, 1986) and on land (e.g. Bamford 1977). Unfortunately, experiments of this kind are prohibitively expensive if the depth range corresponding to the continental upper mantle is considered. Moreover, sometimes these expensive observations do not allow us to distinguish between azimuthal anisotropy and lateral heterogeneity in an isotropic medium. A limited lateral resolution is another drawback of these techniques. The other well-known approach is based on the observations of long-period surface waves (e.g. Forsyth 1975; Tanimoto & Anderson 1985; Montagner & Nataf 1986; Montagner & Tanimoto 1990). This method is very powerful when applied on a global scale but its lateral resolution is not sufficient for regional studies.

In this paper, we explore a possibility to constrain the distribution of azimuthal anisotropy with depth by the analysis of particle motion of teleseismic *S*-waves. The idea is that a discontinuity in the anisotropic elastic parameters should give rise to an *S*-to-*P* converted phase. The properties of this phase are completely different from those in an isotropic medium. Thus, the study is closely related to the subject of *P* precursors to teleseismic *S* which has attracted some attention in the literature (e.g. Bath & Stefansson 1966; Jordan & Frazer 1975; Sacks, Snoke & Husebye 1979; Faber & Müller 1980; Baumgardt & Alexander 1984). To our knowledge, however, the observations of such precursors were never interpreted in terms of anisotropy. The structure of the paper is as follows. In Section 2 we discuss the techniques of analysis and inversion of observations. In Sections 3, 4 and 5, examples of applications of these techniques to real data are presented. In Section 5 we discuss our findings.

### 2 METHOD OF INVERSION

The method of inversion is based on the use of the Thomson–Haskell matrix method for computing theoretical seismograms of body waves in anisotropic media. The computer program is described in Kosarev *et al.* (1979). The model medium consists of a stack of plane layers with arbitrary elastic parameters. The incoming plane wave of *SV* or *SH* type arrives from the isotropic half-space underneath the layered medium. The resulting wavefield is recorded at

the free surface. In Fig. 1 we present examples of theoretical seismograms calculated with our program. We used a model where an anisotropic layer in the upper mantle was placed between the isotropic crust and isotropic mantle. The anisotropic layer is hexagonally anisotropic with a horizontal axis of symmetry. The parameters of the model are given in Table 1. In the synthetics, the primary *SV*- and *SH*-waves split into two quasi-shear waves that present a time delay which is almost independent of the azimuth. The form of the radial motion in *S* associated with the *SV* or *SH* excitation is very close to that in the vertical component. The effect of discontinuities could be demonstrated by calculating the principal direction of the particle motion in the vertical plane and projecting the record on the axis *SV* corresponding to this direction and the orthogonal axis *P*. The *P* component is formed by the *S*-to-*P* converted phases at the two discontinuities and a few multiple reflections. Let us remark that the strongest *P* precursor in Fig. 1 corresponds to the crust-mantle discontinuity. The converted phases depend on the azimuth; the variability is especially strong for the *SH* excitation. This variability is a distinctive feature of an anisotropic medium: in an isotropic (and laterally homogeneous) medium the converted phase is independent of the azimuth and is coupled only with *SV*.

Our strategy of inversion of the observation is as follows. From the observed horizontal components of *S* and a given

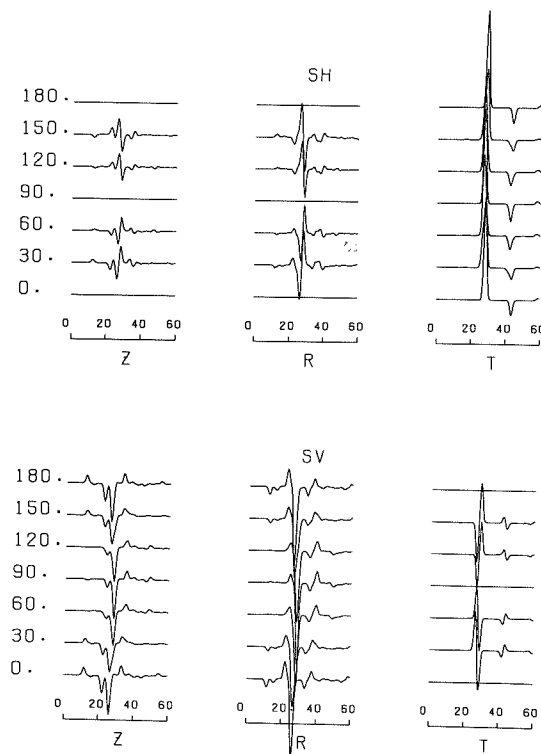


**Figure 1.** Example of theoretical seismograms obtained on the free surface for incident *SH*- (top) and *SV*-waves (bottom). The medium consists of an anisotropic layer placed between the isotropic crust and the isotropic mantle (Table 1). The ray parameter is 12 s degree<sup>-1</sup>. Numbers on the left indicate the angle between the axis of symmetry of the anisotropic layer and the horizontal projection of the wave propagation direction. Time marks indicate second.

**Table 1.** Model used for simulating *Sp* conversion.

Layer 1: Isotropic crust			
Thickness	$V_p$	$V_s$	$\rho$
(km)	(km/s)	(km/s)	(g/cm <sup>3</sup> )
30.	6.20	3.60	2.80

Layer 2: Elastic constants ( $\times 10^{10}$ N m <sup>-2</sup> ) for the anisotropic layer						
Thickness	A	C	L	N	F	$\rho$
(km)						(g/cm <sup>3</sup> )
90.	19.621	23.741	7.151	6.486	5.479	3.38

Layer 3: isotropic half space		
$V_p$	$V_s$	$\rho$
(km/s)	(km/s)	(g/cm <sup>3</sup> )
8.00	4.49	3.38

model of the medium we calculate the theoretical vertical component or, sometimes, the *P* component. We then compare the vertical or *P* components of the observed and calculated records. We assume a number of models; the optimum model minimizes the difference between the observed and calculated components. The method of calculation of the synthetic vertical component is as follows. We denote by  $SV_0$  and  $SH_0$  the *SV* and *SH* amplitudes of the incoming *S*-wave. We assume that no other type of wave is arriving at the same time under the stack of layers. The components of motion recorded at the free surface can be expressed in the frequency domain as

$$\begin{pmatrix} R(\omega) \\ T(\omega) \\ Z(\omega) \end{pmatrix} = \mathbf{F}(\omega) \begin{pmatrix} SV_0(\omega) \\ SH_0(\omega) \end{pmatrix}, \quad (1)$$

where  $R(\omega)$ ,  $T(\omega)$  and  $Z(\omega)$  are the spectra of the recorded radial, transverse and vertical components, respectively. The matrix  $\mathbf{F}(\omega)$  contains the transfer functions which are obtained by the Thomson-Haskell method. This matrix can be written explicitly as

$$\mathbf{F}(\omega) = \begin{pmatrix} R_{SV}(\omega) & R_{SH}(\omega) \\ T_{SV}(\omega) & T_{SH}(\omega) \\ Z_{SV}(\omega) & Z_{SH}(\omega) \end{pmatrix}. \quad (2)$$

From the first two equations of the system (1), we can obtain  $SV_0$  and  $SH_0$  as a function of observed *R* and *T*:

$$\begin{pmatrix} SV_0(\omega) \\ SH_0(\omega) \end{pmatrix} = \frac{1}{R_{SV}(\omega)T_{SH}(\omega) - T_{SV}(\omega)R_{SH}(\omega)} \times \begin{pmatrix} T_{SH}(\omega) & -R_{SH}(\omega) \\ -T_{SV}(\omega) & R_{SV}(\omega) \end{pmatrix} \begin{pmatrix} R(\omega) \\ T(\omega) \end{pmatrix}. \quad (3)$$

This solution is used in the third equation of system (1) in order to obtain the theoretical vertical component denoted  $Z^*(\omega)$ :

$$Z^*(\omega) = Z_{SV}(\omega)SV_0(\omega) + Z_{SH}(\omega)SH_0(\omega). \quad (4)$$

In the time domain,  $Z^*(t)$  is obtained by inverse Fourier transformation.

Similar equations for the *P* component can be written by replacing in equations (1) to (4) the radial and vertical components by the so-called *SV* and *P* components.

We define the penalty function that we want to minimize as

$$E(\mathbf{m}) = \left( \frac{1}{N} \sum_{\text{events}} \frac{\int [Z(t) - Z^*(t, \mathbf{m})]^2 dt}{\int [R^2(t) + T^2(t) + Z^2(t)] dt} \right)^{1/2}, \quad (5)$$

where  $\mathbf{m}$  represents the parameters defining the model and  $N$  is the number of events. The normalization by the energy of the seismogram in the same time interval guarantees against bias due to the strongest events. The function is calculated for different models in a search for one which minimizes  $E(\mathbf{m})$ .

We limited our study to models with hexagonal symmetry and a horizontal axis of symmetry. Such models seem to describe the properties of the upper mantle rocks with sufficient accuracy (e.g. Estey & Douglas 1986) while they are defined by only five elastic parameters and the direction of the axis of symmetry. Exact values of the parameters can be found for many models of the upper mantle. These models, however, are hypothetical and can vary in space. We selected the values of the parameters as follows. The isotropic component of the model is defined by the values of  $V_p$ ,  $V_s$  and density  $\rho$ . The anisotropic component is defined by the values of  $dV_p$ ,  $dV_s$  and  $\eta$ . For the vertical position of the axis of symmetry the parameters  $V_p$ ,  $V_s$ ,  $dV_p$ ,  $dV_s$  and  $\eta$  are related to the five elastic parameters  $A$ ,  $C$ ,  $F$ ,  $L$  and  $N$  by the following expressions:

$$\frac{C}{\rho} = \left( V_p + \frac{dV_p}{2} \right)^2, \quad \frac{A}{\rho} = \left( V_p - \frac{dV_p}{2} \right)^2,$$

$$\frac{L}{\rho} = \left( V_s + \frac{dV_s}{2} \right)^2, \quad \frac{N}{\rho} = \left( V_s - \frac{dV_s}{2} \right)^2,$$

$$F = \eta(A - 2L).$$

To obtain the model with a horizontal axis of symmetry the elastic tensor is rotated.

The isotropic component was obtained from regional *P* and *S* velocity models known from the literature. For the anisotropic component, we usually assumed  $dV_p/V_p = 0.10$ ,  $dV_s/V_s = 0.05$ ,  $\eta = 1.03$ . Similar values of  $dV_p/V_p$  and  $dV_s/V_s$  are often obtained in seismic experiments. The value of  $\eta$  is poorly defined by the seismic experiments; the adopted value makes the resulting velocity variations look like those in a model composed of 30 per cent of oriented olivine crystals and 70 per cent of olivine with random orientation. Some of our numerical experiments were carried out with the following values of the model parameters:  $dV_p/V_p = 0.05$ ,  $dV_s/V_s = 0.03$ ,  $\eta = 1.03$ . These values are also in the range of the reported data and correspond to rocks with a smaller proportion of oriented anisotropic crystals.

**Table 2.** List of events used in this paper.

Event No.	Date	Time hr min s	Lat. (°)	Lon. (°)	Depth km	Station (°)	Distance (°)	B.az.
1	22 04 80	05 34 14.5	32.10 N	137.7 E	402	GRF	85.7	43.1
2	31 01 73	20 55 53.1	28.20 N	139.2 E	498	NOR	81.7	44.9
3	16 06 89	10 51 21.5	57.75 N	153.99 W	58	WUS	71.7	26.8
4	19 05 89	02 21 56.3	54.30 N	165.57 W	104	WUS	69.8	34.3

### 3 INVERSION OF GRAFENBERG DATA

Figure 2 shows a record of teleseismic *S* obtained at a subarray of the GRF array. The epicentral parameters of the event are given in Table 2. The *S*-wave is approximately polarized as *SH* (the amplitude of the radial component is negligible). A distinct *P* arrival precedes *S* in the vertical component by a few seconds. This precursor is well recorded by all the vertical instruments of the array (Fig. 3). The slowness and the direction of propagation of the precursor are practically equal to those of *S*. In a laterally homogeneous and isotropic medium the *P*-wave is coupled only with *SV*; the theoretical amplitude ratio between the *SV*-to-*P* conversion and the vertical component of *SV* for conversion at the crust/mantle boundary is around 0.2. The *S* velocity contrasts at the other discontinuities in the lithosphere are much lower than at the crust-mantle boundary; the corresponding conversions should be weaker in nearly the same proportion. The precursor in Fig. 2 is clearly too strong to be explained by conversion from *SV* to *P* underneath the station.

The other possibility which could be considered for explaining the precursor is conversion from *SH* to *P* at a dipping crust-mantle boundary. It can be shown, however, that this is unlikely. The strongest coupling between *SH* and *P* occurs if the strike of the dipping interface is in the vertical plane containing the source and the receiver. Then the coefficient of transmission from *SH* to *P* at the dipping interface  $C_{SH}$  can be expressed approximately as follows

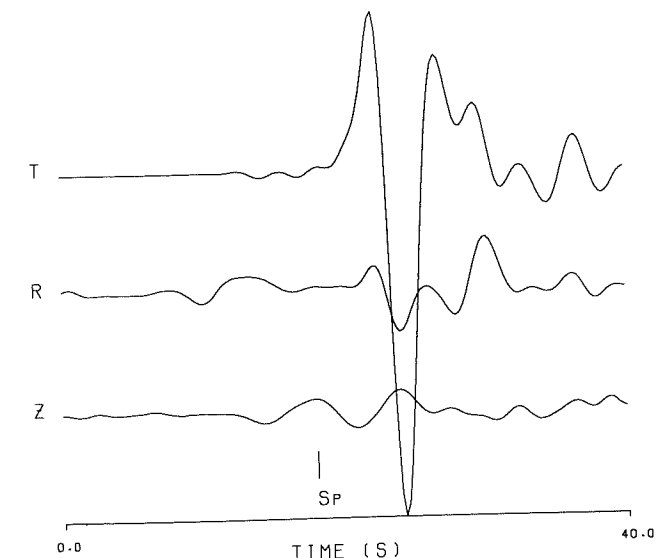


**Figure 2.** Example of an *S*-wave observation for event 1 recorded at the subarray  $A_1$  of the GRF array. The horizontal component records have been rotated to radial (*R*) and transverse (*T*). (*Z*) Vertical; (*R*) radial; (*T*) transverse. The mark *Sp* corresponds to the maximum displacement in the precursor.



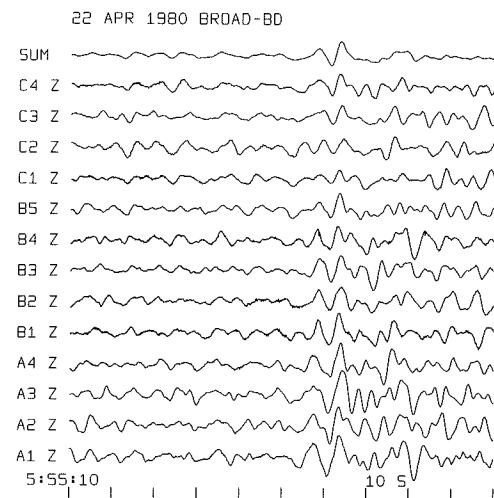


Figure 3. Records obtained at all the vertical component instruments of the GRF array for event 1. The records are aligned (slowness is 8.4 s degree<sup>-1</sup>) and summed (trace sum). The precursor to *S* arrives at 5 h 56 m 5 s.

(see Appendix):

$$C_{SH} = C_{SV}(i) \cos(g) \quad (6)$$

where

$$\cos(g) = \frac{\tan(f)}{\sqrt{\cos^2(e) + \tan^2(f)}}$$

and

$$\cos(i) = \cos(f) \sin(e),$$

where  $C_{SV}$  is the coefficient of transmission from *SV* to *P* obtained for the incidence angle  $i$  with respect to the interface,  $e$  is the angle of emergence of *SH* with respect to the horizontal plane and  $f$  is the dip of the plane of conversion (see Appendix). The observed ratio between the primary *SH* and the vertical component of *Sp* is close to 0.08. To explain the amplitude of the precursor by a dipping Moho, the value of  $\cos(g)$  should be close to 0.8. Adopting  $e = 70^\circ$  and  $f = 10^\circ, 15^\circ$  and  $20^\circ$  we find that  $\cos(g)$  is equal to 0.46, 0.62 and 0.73, respectively. Thus the smallest acceptable values of  $f$  are around  $20^\circ$  implying that the depth of Moho underneath the array which is nearly 100 km long should vary in the range of 20 km. The real variations, however, are by an order of magnitude smaller (Liu & Kind 1986). It could be shown also that the measured back azimuth of the converted phase would differ from that in Table 2 by  $15^\circ$ . The observed difference, however, is smaller by an order of magnitude. Thus the generation of the precursor by the dipping interface in the isotropic Earth is practically impossible.

We should also consider a possibility of generating the precursor by multiple surface reflections *PP*..., *PPP*..., and *sPPP*..., or scattering from *S* to *P* in the lithosphere between the source and the receiver (seismic phase *S.P* and *SP.P*, see Vinnik & Romanowicz 1990). The first possibility is unlikely since for the given epicentral parameters only *sPPP*... may arrive in the time interval of *S*. The multiple reflections form a sequence of phases following one after the other with an interval of 20–35 s. As shown in Fig. 3, this

sequence is not present in the record. This can be explained either by the radiation pattern of the source or by the fact that the energy of these phases is concentrated in the longer period band, due to their very long traveltime in the low-*Q* asthenosphere. The second possibility is unlikely for several reasons. Firstly, the slowness of the scattered precursor must be by 1 s degree<sup>-1</sup> lower than that of *S*; in reality both values are practically the same. Secondly, the theoretical amplitude ratio between the precursor and *S* which is calculated by using the same method as in Vinnik & Romanowicz (1990) is 20 times smaller than the observed ratio. Thirdly, the signal is well correlated across the array which is unlikely to be the case for a scattered wavefield.

A remaining possibility is the generation of the precursor in a medium with azimuthal anisotropy. A discontinuity in the anisotropic parameters gives rise to an *SH*-to-*P* conversion (see Fig. 1). To substantiate this we started from a simple model with one homogeneous anisotropic layer between the top of the mantle and a depth of 54 km. The parameters of the model are given in Table 3. Fig. 4 shows the synthetic vertical component  $Z^*(t)$  as a function of azimuth of the axis of fast velocity. The principal features of the synthetics are related to conversion from *S* to *P* at the discontinuity between the isotropic half-space and the anisotropic layer. In general, the agreement between the observation and the synthetics is poor, though some improvement is obtained for the azimuth of fast velocity near  $0^\circ$ . Moreover, this direction is in sharp disagreement with the direction of  $90^\circ$  which was obtained from the observations of *SKS* (Vinnik *et al.* 1989). We conclude that the simple model of Table 3 is unacceptable.

To go one step further in the inversion of the data, we assumed a more complicated model where the upper mantle consists of a thick anisotropic layer with the axis fixed at  $90^\circ$  east from north (in agreement with the *SKS* data) and a relatively thin anisotropic layer at the top of the mantle. The synthetic vertical components  $Z^*(t)$  corresponding to different azimuths of the axis of fast velocity in the upper layer are shown in Fig. 5. The optimum direction of the axis in the upper layer was found by trial and error. The best agreement between the synthetics and the observed record is obtained for the azimuth between  $0^\circ$  and  $20^\circ$ . The parameters of the two-layer model are given in Table 3. In Fig. 6 we present enlarged records of the observed vertical component (A), the synthetic for the optimum azimuth (B) and the synthetic corresponding to the isotropic model given in Table 3 (C). This isotropic model has a strong shear velocity contrast, but the corresponding converted phase is very weak. This comparison shows very good agreement between the observed and synthetic vertical components for the two-layer anisotropic model. In the two-layer model the effective direction of the axis which can be found from *SKS* is slightly less than  $90^\circ$ . This change could be accounted for by a slight change in the direction of axis in the lower anisotropic layer. We have studied the influence of the direction of axis in the lower anisotropic layer on the value of the penalty function. Fig. 7 shows the contours of the penalty function  $E(\phi_1, \phi_2)$  as a function of the azimuths  $\phi_1$  and  $\phi_2$  of the axis in the two anisotropic layers. The minimum corresponds to  $\phi_1 = 0^\circ$  and  $\phi_2 = 90^\circ$ , which corresponds to the two-layer model described in Table 3.

Let us discuss the influence of other parameters. The

Table 3. Models used for simulating *Sp* conversion at GRF.

One layer model					$dV_P/V_P$	$dV_S/V_S$	$\eta$	$\phi$
Layer	Thickness (km)	$V_P$ (km s <sup>-1</sup> )	$V_S$ (km s <sup>-1</sup> )	$\rho$ (g cm <sup>-3</sup> )				
1	27	5.80	3.20	2.60	0.00	0.00	1.00	$\phi_1 = 0^\circ$
2	27	7.90	4.39	3.31	0.00	0.00	1.00	
3	$\infty$	8.00	4.49	3.38	0.05	0.03	1.03	
4	$\infty$	8.00	4.49	3.38	0.00	0.00	1.00	
Two layer model					$dV_P/V_P$	$dV_S/V_S$	$\eta$	$\phi$
Layer	Thickness (km)	$V_P$ (km s <sup>-1</sup> )	$V_S$ (km s <sup>-1</sup> )	$\rho$ (g cm <sup>3</sup> )				
1	27	5.80	3.20	2.60	0.00	0.00	1.00	$\phi_1 = 0^\circ$
2	27	7.90	4.39	3.31	0.00	0.00	1.00	
3	166	8.00	4.49	3.38	0.10	0.05	1.03	$\phi_2 = 90^\circ$
4	$\infty$	8.00	4.49	3.38	0.05	0.03	1.03	
5	$\infty$	8.56	4.54	3.44	0.00	0.00	1.00	
Isotropic model					$dV_P/V_P$	$dV_S/V_S$	$\eta$	$\phi$
Layer	Thickness (km)	$V_P$ (km s <sup>-1</sup> )	$V_S$ (km s <sup>-1</sup> )	$\rho$ (g cm <sup>3</sup> )				
1	27	5.80	3.20	2.60	0.00	0.00	1.00	$\phi_1 = 0^\circ$
2	27	7.90	4.39	3.31	0.00	0.00	1.00	
3	$\infty$	8.00	4.49	3.38	0.05	0.03	1.03	$\phi_2 = 90^\circ$
4	$\infty$	8.56	4.54	3.44	0.00	0.00	1.00	

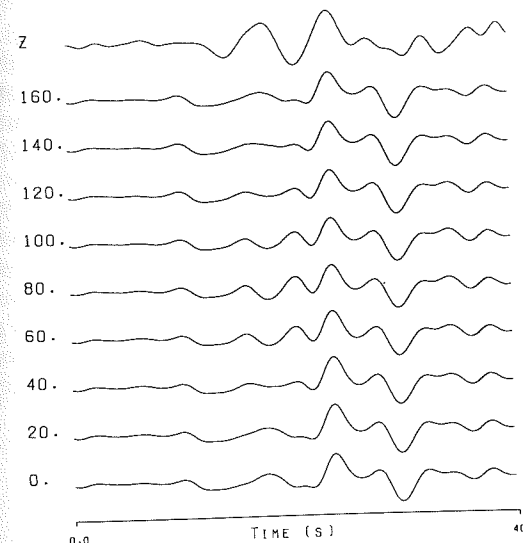


Figure 4. Synthetic vertical components at GRF for the one layer anisotropic model given in Table 3 as a function of azimuth of the axis of fast velocity. Observed vertical component is also shown (*Z* trace). Ray parameter used in the calculation is 8.5 s degree<sup>-1</sup>. Numbers on the left indicate the azimuth of fast axis.

depth of the interface between the two anisotropic layers is well constrained: it is determined by the time difference between the precursor and the *S*-wave. The amplitude of the precursor is related to the anisotropic parameters of the two anisotropic layers by the transmission coefficient of *S* to *P* at the interface. However, numerical experiments show that the data is neither sensitive to the parameter  $\eta$  nor to the thickness of the lower anisotropic layer.

Propagation in anisotropic models causes coupling between *SV* and *SH* components. Fig. 8 shows the *SV*<sub>0</sub> and

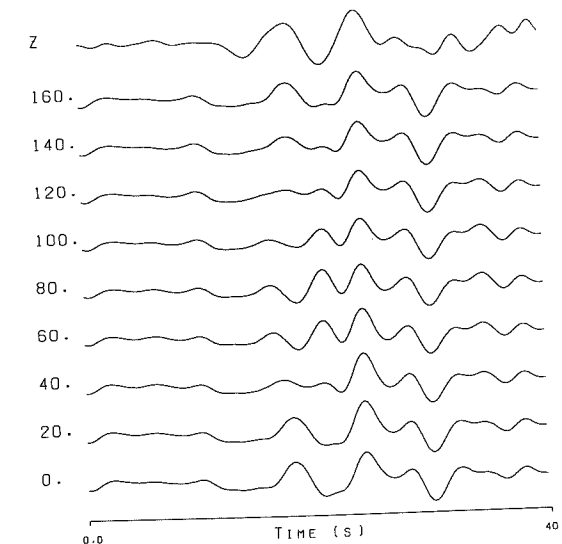


Figure 5. Synthetical vertical components at GRF for the two-layer anisotropic model shown in Table 3 as a function of azimuth  $\phi_1$  of the axis of fast velocity in the first layer. The azimuth  $\phi_2$  of fast velocity in the lower layer is fixed at  $\phi_2 = 90^\circ$ . Observed vertical component is also shown (*Z* trace). Numbers on the left indicate the azimuth of fast axis  $\phi_1$ .

*SH*<sub>0</sub> time series corresponding to the two layer model with the optimum parameters (Table 3). They were obtained by using equation (3). One can see that energy is present on the incident *SV* component and that the ratio *SH*/*SV* obtained at the bottom of the model is quite different from the observed *T/R* ratio of the *S*-wave. This phenomenon is a consequence of shear wave splitting which causes destructive interference of the *SV* component.

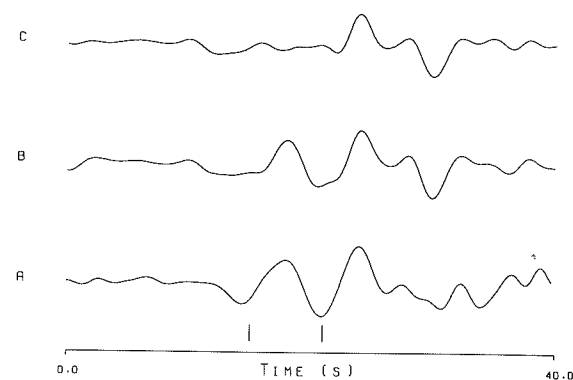


Figure 6. Comparison of observed and synthetics obtained at station GRF. (A) Observed vertical component. (B) Synthetic vertical component obtained for the two-layer anisotropic model given in Table 3. (C) Synthetic Z component for the isotropic model given in Table 3. Vertical bars indicate the time window used in the penalty function calculation.

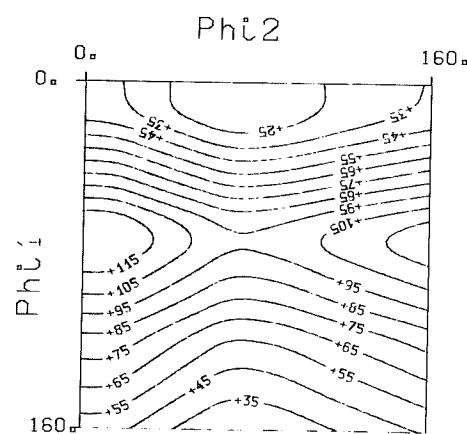


Figure 7. Plot of contours of residuals versus angles  $\phi_1$  and  $\phi_2$  at station GRF obtained using event 1.  $\phi_1$  and  $\phi_2$  are the azimuths of the axis of fast velocity in the two anisotropic layers.

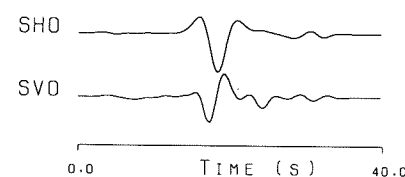


Figure 8.  $SV_0$  and  $SH_0$  time series obtained for event 1 using the two-layer model given in Table 3.

#### 4 INVERSION OF NORSAR DATA

At NORSAR, precursors to teleseismic  $S$  were reported by Sacks *et al.* (1979). The authors argued that this precursor is a converted phase rather than a multiple surface reflection. They presented evidence showing that the arrival of the precursor is associated with a sharp increase in observed slowness, whereas, before the precursor offset, the slowness is low, corresponding to multiples. In our view, the most convincing evidence presented by Sacks *et al.* (1979) in favour of the hypothesis of conversion is the similarity

between records from events with different depths and slightly different back azimuths and epicentral distances. Although we agree with Sacks *et al.* (1979) that the precursor could be due to  $S$ -to- $P$  conversion, we do not think that it could be generated at discontinuities in an isotropic Earth.

We could not obtain the original records and limited our analysis to the three-component record of one event reproduced in Fig. 7 of the paper by Sacks *et al.* (1979) as a representative example of their data. Epicentral parameters of the event are listed in Table 2. The digitized copy of the record is reproduced in our Fig. 9. It is clear that the radial component of  $S$  is much smaller than the transverse one; in other words, the  $S$ -wave is polarized almost as  $SH$ . The amplitude ratio between the precursor and the vertical component of  $S$  is close to unity. Repeating the arguments which were presented in the discussion of the GRF data, one can easily show that this ratio is too high for the converted phase  $SV_p$ . Very high values of this ratio are also evident in the other examples of vertical component data which are shown in Fig. 6 of Sacks *et al.* (1979).

The impossibility to explain the precursor by conversion from  $SV$  to  $P$  implies that it could be generated by conversion from  $SH$  to  $P$ . Such conversion is possible either at a dipping interface in an isotropic medium or at a boundary between anisotropic media. The former possibility, however, is unlikely. Using equation (6), we can explain the amplitude ratio between the precursor and  $SH$  (around 0.1) by conversion at a dipping interface if the shear velocity contrast at this discontinuity is about  $1.0 \text{ km s}^{-1}$ . Such a strong discontinuity at a depth near 250 km where this conversion occurs is unrealistic.

Exploring a possibility to explain the data in Fig. 9 by azimuthal anisotropy, we projected the record on the axes  $P$  and  $SV$  and assumed a model whose isotropic component in the depth range around 250 km resembles other known models of the Lehman discontinuity. We found by trial and error that the amplitude of the precursor is too large to be explained by conversion at a discontinuity between isotropic

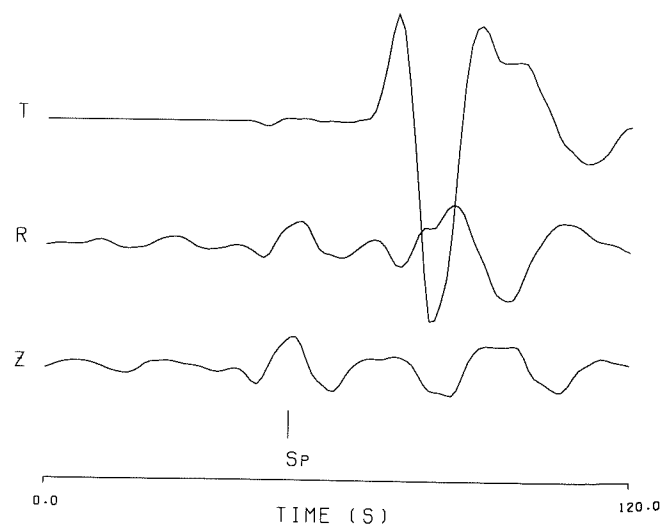


Figure 9. Example of  $S$ -wave observation for event 2 recorded at NORSAR. The horizontal component records have been rotated to radial ( $R$ ) and transverse ( $T$ ).

Table 4. Models used for simulating  $Sp$  conversion at NORSAR.

Two layer model for NORSAR					$dV_p/V_p$	$dV_s/V_s$	$\eta$	$\phi$
Layer	Thickness (km)	$V_p$ ( $\text{km s}^{-1}$ )	$V_s$ ( $\text{km s}^{-1}$ )	$\rho$ ( $\text{g cm}^{-3}$ )				
1	40	6.20	3.60	2.80	0.00	0.00	1.00	$\phi_1 = 20^\circ$ $\phi_2 = 90^\circ$
2	120	8.3	4.6	3.38	0.00	0.00	1.00	
3	60	8.3	4.6	3.38	0.10	0.05	1.03	
4	60	8.7	4.8	3.50	0.10	0.05	1.03	
5	$\infty$	8.7	4.8	3.50	0.00	0.00	1.00	
Isotropic model					$dV_p/V_p$	$dV_s/V_s$	$\eta$	$\phi$
Layer	Thickness (km)	$V_p$ ( $\text{km s}^{-1}$ )	$V_s$ ( $\text{km s}^{-1}$ )	$\rho$ ( $\text{g cm}^{-3}$ )				
1	40	6.20	3.60	2.80				
2	180	8.3	4.6	3.38				
3	$\infty$	7.0	4.0	3.00				

and anisotropic media. In principle this is possible but the required magnitude of anisotropy is seldom found in the upper mantle rocks. For this reason, we prefer a model with a discontinuity between two anisotropic layers with different directions of fast axes. Table 4 presents the parameters of the model we chose. Fig. 10 demonstrates the sensitivity of the synthetic  $P$  component to the direction of the axis in the upper layer. The direction in the lower layer is fixed at  $90^\circ$  whereas the direction in the upper layer is variable; a good fit is observed for a relatively narrow range of azimuths near  $20^\circ$ . Fig. 11 shows enlarged records of the  $P$  component corresponding to the observed records and synthetics for the optimum parameters and for the isotropic model given in Table 4. This isotropic model has a strong shear velocity contrast. It is clear that in the isotropic model the converted phase is too weak whereas the anisotropic model explains the observed amplitude quite well. Fig. 12 shows the

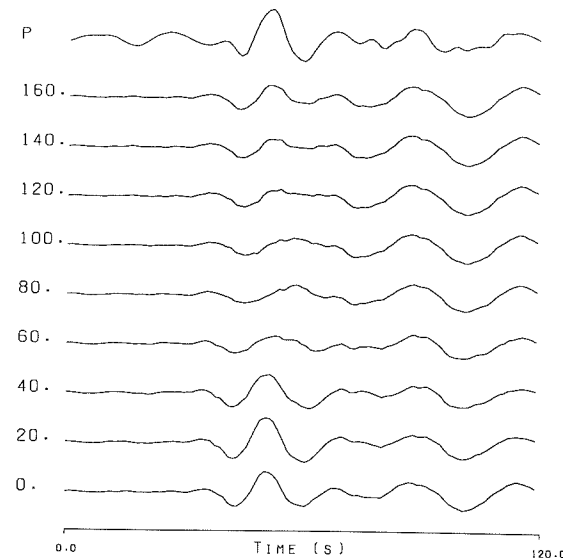


Figure 10. Synthetic  $P$  components for NORSAR versus azimuth  $\phi_1$  of axis of fast velocity in the upper anisotropic layer. The azimuth  $\phi_2$  of the axis in the lower anisotropic layer is fixed at  $90^\circ$ . The corresponding model is given in Table 4. The observed  $P$  component is also shown ( $P$  trace). The ray parameter used in the calculation is  $12.0 \text{ s degree}^{-1}$ . Numbers on the left indicate the azimuth of fast axis  $\phi_1$ .

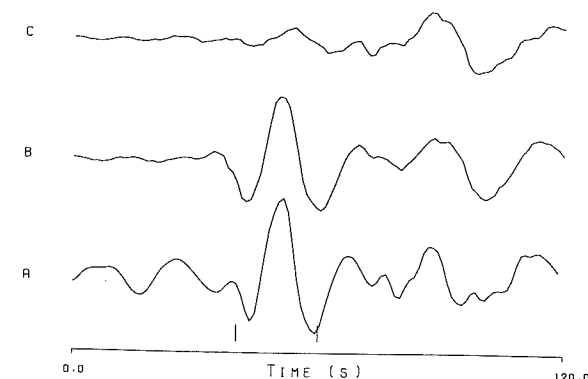


Figure 11. Comparison of observed and synthetics obtained at NORSAR. (A) Observed  $P$  component. (B) Synthetic  $P$  component obtained for the two-layer model given in Table 4. (C) Synthetic  $P$  component for the isotropic model given in Table 4. Vertical bars indicate the time window used in the penalty function calculation.

sensitivity of data to the azimuths  $\phi_1$  and  $\phi_2$  of the axis of fast velocity in the two anisotropic layers. One can see a clear minimum at  $\phi_1 = 20^\circ$  and  $\phi_2 = 90^\circ$ , which corresponds to the model described in Table 4.

Let us discuss the influence of other parameters. As in the case of Grafenberg, the depth of the interface between the

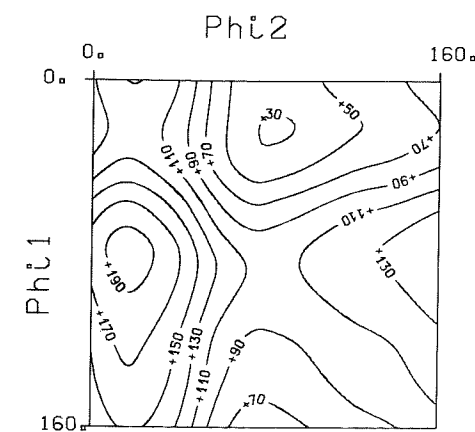


Figure 12. Plot of contours of residuals versus angles  $\phi_1$  and  $\phi_2$  at NORSAR obtained using event 2.  $\phi_1$  and  $\phi_2$  are the azimuths of the axis of fast velocity in the two anisotropic layers.

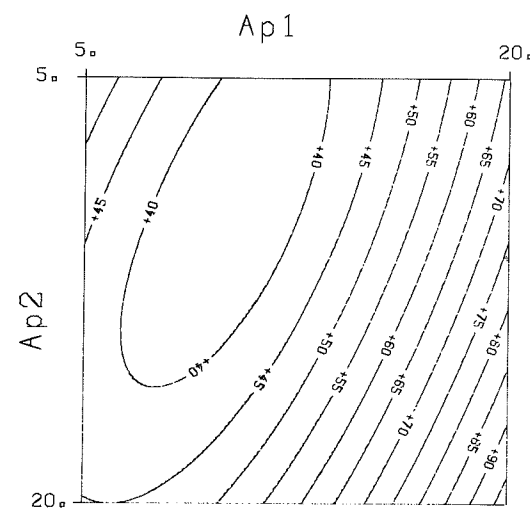


Figure 13. Plot of contours of residuals versus the values of the anisotropy parameter  $A_p = 100 dV_P/V_P$  in the two layers obtained using event 2.

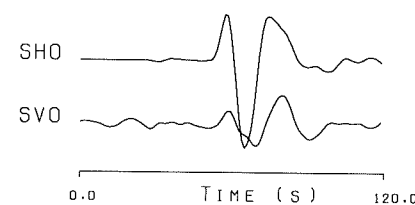


Figure 14.  $SV_0$  and  $SH_0$  time series obtained for event 2 using the two-layer model given in Table 4.

two anisotropic layers is determined by the time difference between the precursor and the  $S$ -wave. The thickness of the two layers is related to the width of the precursor. Numerical experiments show that the data is neither sensitive to the parameter  $\eta$  nor to the value of  $dV_S/V_S$  in the two anisotropic layers. However, the value of  $dV_P/V_P$  in the two layers is constrained by the data. Fig. 13 shows the sensitivity of data to the values of this parameter in the two layers (the other parameters being the same as in Table 4). One can see a clear minimum when the parameter  $dV_P/V_P = 0.10$  in the two layers.

Let us now look at the effect of the anisotropic model on the  $S$ -wave. Fig. 14 shows the  $SV_0$  and  $SH_0$  time series obtained for the two-layer model with optimum parameters (Table 4). One can see that there is almost no change in the waveform of  $SH_0$  and  $SV_0$  when compared with the observed transverse and radial components of the  $S$ -wave in Fig. 9. The  $SV/SH$  ratio has been hardly modified by the anisotropic model. At  $45^\circ$  of the two symmetry axes, anisotropy effects of the two layers on the  $S$ -wave cancel each other. The precursor on the radial component has been interpreted by the model as an  $SH$ -to- $P$  conversion.

## 5 WESTERN CHINA

For the station WUS of the GEOSCOPE network (western China; lat. =  $41.2^\circ$ , long. =  $79.2^\circ$ ) we inverted simultaneously two records. The time span of operation available for this station, which was installed in October 1988 (Romanowicz et al. 1991), is about half a year. For this reason, it was

impossible to find records with  $SH$  amplitude stronger than the  $SV$  amplitude. We worked with records where the amplitude of  $SH$  is lower than the amplitude of  $SV$ . The observations of  $SKS$  for this station indicate that the direction of fast velocity is near  $80^\circ$  and  $\delta t$  is near 1.2 s (Taiki, private communication). The records of  $S$  precursors are displayed in Fig. 15. For event 3, the transverse component of the  $S$ -wave looks like the time derivative of the radial component. This effect may be compared to the effect of an anisotropic layer on the incident  $SV$ -wave in Fig. 1. These data were inverted by using an iterative procedure. In the first step, we considered a model with one anisotropic layer between the isotropic crust and a half-space which was found to explain some features in the seismograms. However, the first motion in the precursor

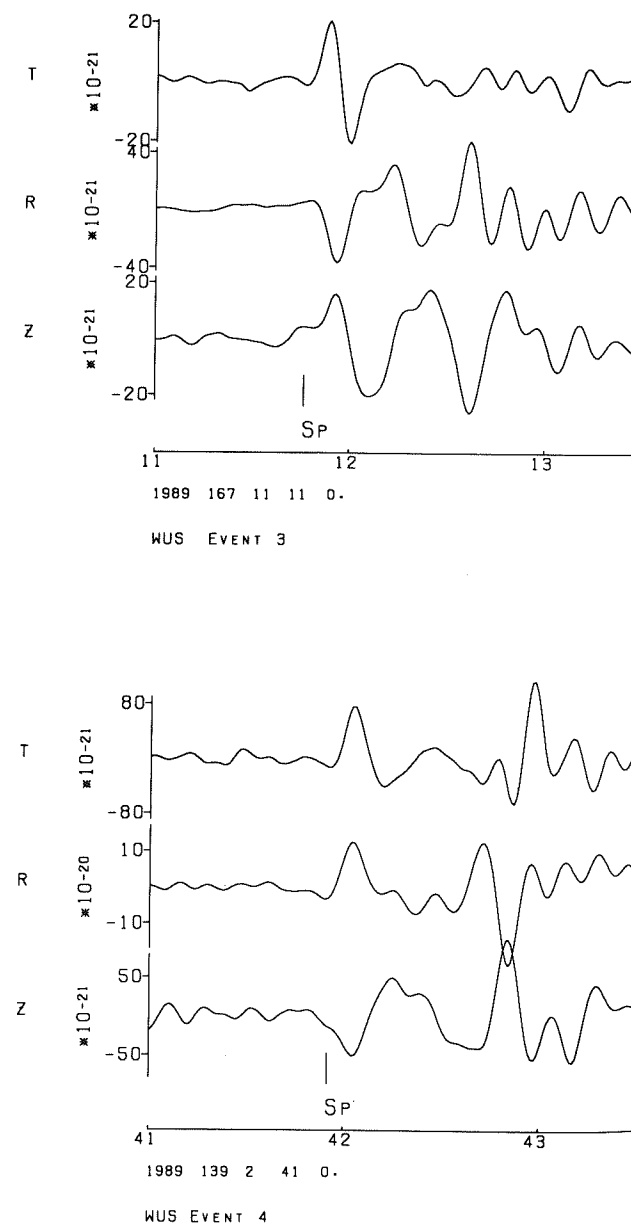


Figure 15. Examples of  $S$ -wave observations recorded at station WUS. The horizontal component records have been rotated to radial ( $R$ ) and transverse ( $T$ ). Time marks are minutes.

Table 5. Model used for simulating  $Sp$  conversion at WUS.

Two layer model for WUS					$dV_P/V_P$	$dV_S/V_S$	$\eta$	$\phi$
Layer	Thickness (km)	$V_P$ (km s $^{-1}$ )	$V_S$ (km s $^{-1}$ )	$\rho$ (g cm $^{-3}$ )				
1	45	6.20	3.60	2.80	0.00	0.00	1.00	
2	35	8.0	4.49	3.38	0.10	0.05	1.03	$\phi_1 = 110^\circ$
3	90	8.0	4.49	3.38	0.10	0.05	1.03	$\phi_2 = 60^\circ$
4	$\infty$	8.0	4.49	3.38	0.00	0.00	1.00	

starts several seconds earlier than the conversion at the Moho can explain. In the next step, we used a model where the upper mantle consists of two anisotropic layers with a boundary at 80 km depth (Table 5). Fig. 16 shows the synthetic vertical components  $Z^*(t)$  for event 3 as a function of the azimuth  $\phi_1$  of the axis of fast velocity in the upper layer (the axis of fast velocity in the lower layer is fixed at  $\phi_2 = 60^\circ$ ). The best fit to the observation is provided by the direction  $110^\circ$  in the upper layer and  $60^\circ$  in the lower layer. The effective direction corresponding to  $SKS$  data is near  $80^\circ$  which is close to the observed one. Fig. 17 shows the theoretical and observed vertical components for the two events. The fit is nearly perfect. Fig. 18 shows the contours of the penalty function versus the azimuths  $\phi_1$  and  $\phi_2$  of the axis of fast velocity in the two anisotropic layers. One can see a clear minimum at  $\phi_1 = 110^\circ$  and  $\phi_2 = 60^\circ$ , which corresponds to the model described in Table 5.

Let us discuss the influence of other parameters. As in the case of Grafenberg, the depth of the interface between the

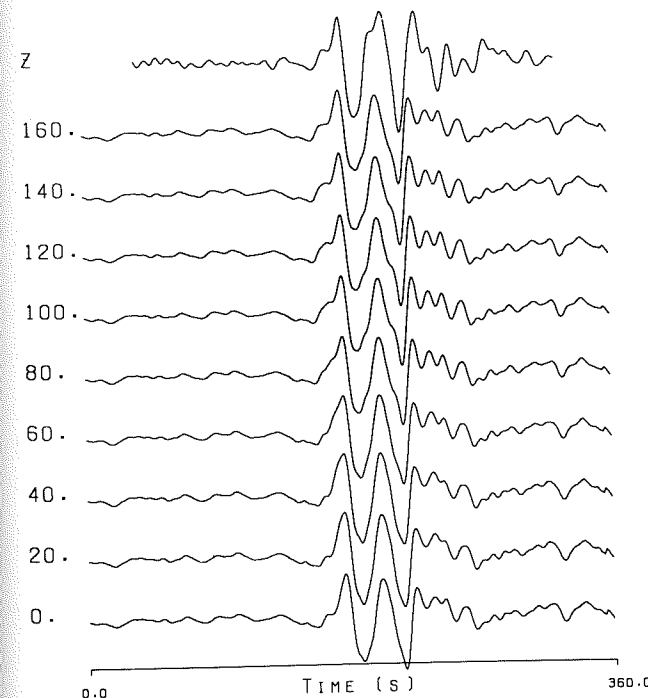


Figure 16. Synthetic vertical components obtained for event 3 at WUS as a function of azimuth  $\phi_1$  of the axis of fast velocity in the upper layer. The azimuth  $\phi_2$  of the axis in the lower anisotropic layer is fixed at  $\phi_2 = 60^\circ$ . The model is given in Table 5. Observed vertical component is also shown ( $Z$  trace). Numbers on the left indicate the azimuth of fast axis  $\phi_1$ .

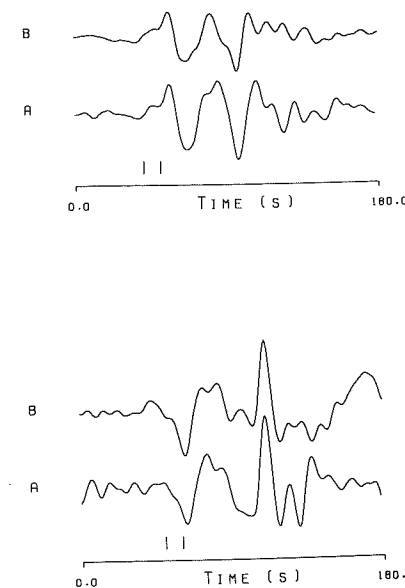


Figure 17. Comparison of observed and synthetics obtained at station WUS for events 3 and 4. (A) Observed vertical component. (B) Synthetic vertical component obtained for the two-layer model given in Table 5. Vertical bars indicate the time window used in the penalty function calculation. Ray parameter used in the calculation is  $11.5 \text{ s degree}^{-1}$  for event 3 and  $11.8 \text{ s degree}^{-1}$  for event 4.

two anisotropic layers is determined by the time difference between the precursor and the  $S$ -wave. Numerical experiments show that the data are not sensitive to the parameter  $\eta$ . The value of the parameters  $dV_P/V_P$  and  $dV_S/V_S$  in the upper anisotropic layer is not very well

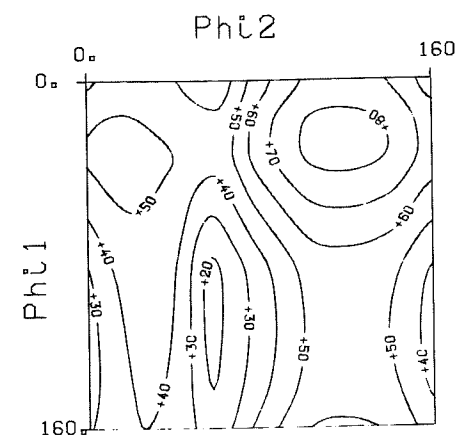


Figure 18. Plot of contours of residuals versus angles  $\phi_1$  and  $\phi_2$  at station WUS obtained using events 3 and 4.  $\phi_1$  and  $\phi_2$  are the azimuths of the axis of fast velocity in the two anisotropic layers.



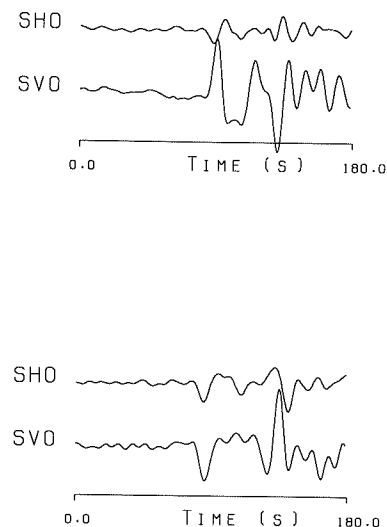


Figure 19.  $SV_0$  and  $SH_0$  time series obtained for event 3 and 4 using the two-layer model given in Table 5.

constrained. In the lower anisotropic layer, the data are principally sensitive to the parameter  $dV_P/V_P$ .

Figure 19 shows the  $SV_0$  and  $SH_0$  time series obtained for the two events by using the model with the optimum parameters (Table 5). There is almost no effect of the anisotropic model on the  $S$  components of the event 4. For event 3, the incident  $S$ -wave is almost polarized as an  $SV$ -wave and the observed transverse component can be explained as an effect of the propagation in the anisotropic medium.

## 6 DISCUSSION AND CONCLUSIONS

We described a technique for the inversion of  $S$ -wave particle motion in terms of azimuthal anisotropy in the lithosphere. In some respects, this method resembles the technique of crustal receiver-function analysis but is more complicated. The technique exploits coupling between  $SH$ ,  $SV$  and  $P$  which is characteristic of media with azimuthal anisotropy. There is a problem of discriminating between conversions at dipping interfaces in isotropic media and horizontal interfaces in the presence of azimuthal anisotropy. We presented examples of seismic observations where the data are clearly in favour of an anisotropic model. These data were used to test the feasibility of the method. We believe that the results of these tests are encouraging.

From the GRF data we found a two-layered anisotropic model for the upper mantle. This model eliminates the apparent incompatibility between the  $SKS$  data which indicate a fast velocity azimuth near  $90^\circ$  (Vinnik *et al.* 1989) and deep seismic sounding results for the same region indicating a direction close to  $20^\circ$  (Bamford 1977). It should be stressed that the two-layered model was constructed without any special effort to explain the deep seismic sounding results. The origin of this two-layer structure can perhaps be explained using the rock physics data (e.g. Estey & Douglas 1986). Anisotropy in the upper mantle is explained by crystallographic mineral alignment which is associated with upper mantle shear flow. Mobility of the upper mantle rocks is enhanced by high temperature; the threshold temperature of enhanced mobility is 1100–1200 K.

Anisotropy in the upper, relatively cold layer of our model could be in a fossil state whereas anisotropy in the lower layer could be due to contemporary flow in the asthenosphere. The direction of  $90^\circ$  in the lower layer is nearly parallel to the strike of the Alpine belt. We also note that the discontinuity between the two layers could correspond to the spinel to garnet phase transformation in the ultramafic mantle material (Vinnik 1989). These possibilities could be tested using other data on the deep structure and tectonics of the region.

For NORSAR, we obtained a model where the Lehman discontinuity is a boundary between anisotropic media with different directions of fast axes. There are some other indications of anisotropy at this discontinuity. Leven, Jackson & Ringwood (1981) interpreted  $P$ -wave refraction data for Australia in terms of azimuthal anisotropy; they suggested that this anisotropy is produced by a differential motion in a zone of transition from the lithosphere to the asthenosphere. Estey & Douglas (1986) proposed that the Lehman discontinuity is due to a change from pyrolyte with a strong azimuthal anisotropy to practically isotropic piclogite. The parameters of our model for NORSAR are less well constrained than those for the GRF model. However, there are many other sources of information which could be used in the future to put additional constraints on these parameters. The most obvious of them are the records of  $SKS$  and the records of  $S$  polarized in many different directions.

In the case of station WUS, in western Xinkiang, we may also interpret our observations in term of two anisotropic layers with different directions of fast axes. The anisotropy in the upper layer could be in a fossil state while the direction of anisotropy in the lower layer could be formed recently. This explanation is supported by the fact that the direction of  $60^\circ$  in the lower layer is nearly parallel to the strike of the Tien Chan mountain range. Like in the case of GRF, the boundary between the two anisotropic layers could correspond to spinel to garnet phase transformation.

Constructing models with depth-dependent anisotropy is an iterative process where many high-quality recordings are required. Our models which are based on a small number of data can be regarded as a crude approximation to real structures. However, the experience of constructing these models makes us believe that our approach is feasible and can be used in future studies of the earth interior and will help to put constraints on present and past dynamics of the upper mantle.

## ACKNOWLEDGMENTS

We thank R. Madariaga and an anonymous reviewer for very stimulating reviews. This research was conducted while L. Vinnik was a visiting scientist at IPG. IPGP contribution no. 1160.

## REFERENCES

- Bamford, D., 1977.  $P_n$ -velocity anisotropy of the uppermost mantle under oceans, *Geophys. J. R. astr. Soc.*, **49**, 29–48.
- Bath, M. & Stefansson, R., 1966.  $S$ – $P$  conversion at the base of the crust, *Ann. Geofis.*, **19**, 119–130.
- Baumgardt, D. R. & Alexander, S. S., 1984. Structure of the mantle beneath Montana LASA from analysis of long period, mode-converted phases, *Bull. seism. Soc. Am.*, **74**, 1683–1707.
- Estey, L. H. & Douglas, B. J., 1986. Upper-mantle anisotropy: A preliminary model, *J. geophys. Res.*, **91**, 11 393–11 406.
- Faber, S. & Müller, G., 1980. Sp phases from the transition zone between the upper and lower mantle, *Bull. seism. Soc. Am.*, **70**, 487–508.
- Forsyth, D. W., 1975. The early structural evolution and anisotropy of the oceanic upper mantle, *Geophys. J. R. astr. Soc.*, **43**, 103–162.
- Hess, H. H., 1964. Seismic anisotropy of the uppermost mantle under oceans, *Nature*, **203**, 629–631.
- Jordan, T. H. & Frazer, L. N., 1975. Crustal and upper mantle structure from Sp phases, *J. geophys. Res.*, **80**, 1504–1518.
- Kind, R., Kosarev, G. L., Makeyeva, L. I. & Vinnik, L. P., 1985. Observations of laterally inhomogeneous anisotropy in the continental lithosphere, *Nature*, **318**, 358–361.
- Kosarev, G. L., Makeyeva, L. I., Savarensky, E. F. & Chesnokov, E. M., 1979. Effect of anisotropy beneath seismic stations on body waves, *Izv. Akad. Nauk. USSR Fiz. Zemli*, **2**, 26–37.
- Leven, J. H., Jackson, I. & Ringwood, A. E., 1981. Upper mantle seismic anisotropy and lithospheric decoupling, *Nature*, **289**, 234–239.
- Liu, Q. Y. & Kind, R., 1986. Lateral variations of the structure of the crust–mantle boundary from conversions of teleseismic P-waves, *J. Geophys.*, **60**, 149–156.
- Montagner, J. P. & Nataf, H. C., 1986. A simple method for inverting the azimuthal anisotropy of surface waves, *J. geophys. Res.*, **91**, 511–520.
- Montagner, J. P. & Tanimoto, T., 1990. Global anisotropy in the upper mantle inferred from the regionalization of phase velocities, *J. geophys. Res.*, **95**, 4797–4820.
- Romanowicz, B. *et al.*, 1991. The GEOSCOPE program: Present status and perspectives, *Bull. seism. Soc. Am.*, **81**, 243–264.
- Sacks, I. S., Snoke, J. A. & Husebye, E. S., 1979. Lithosphere thickness beneath the Baltic shield, *Tectonophysics*, **56**, 101–110.
- Shearer, P. M. & Orcutt, J. A., 1985. Anisotropy in the oceanic lithosphere—Theory and observations from the Ngendei seismic refraction experiment in the southwest Pacific, *Geophys. J. R. astr. Soc.*, **80**, 493–526.
- Shearer, P. M. & Orcutt, J. A., 1986. Compressional and shear wave anisotropy in the oceanic lithosphere—The Ngendei seismic refraction experiment, *Geophys. J. R. astr. Soc.*, **87**, 967–1003.
- Shimamura, H., 1984. Anisotropy in the oceanic lithosphere of the Northwestern Pacific Basin, *Geophys. J. R. astr. Soc.*, **76**, 253–260.
- Silver, P. & Chan, W. W., 1988. Implications for continental structure and evolution from seismic anisotropy, *Nature*, **335**, 34–39.
- Tanimoto, T. & Anderson, D. L., 1985. Lateral heterogeneity and azimuthal anisotropy of the upper mantle: Love and Rayleigh waves 100–250 s, *J. geophys. Res.*, **90**, 1842–1858.
- Vinnik, L. P., 1989. Mantle discontinuities, in *Encyclopedia of the Solid Earth Geophysics*, pp. 802–806, ed. James, D., Van Nostrand Reinhold, New York.
- Vinnik, L. P. & Romanowicz, B., 1990. Origin of precursors to teleseismic S waves, *Bull. seism. Soc. Am.*, submitted.
- Vinnik, L. P., Farra, V. & Romanowicz, B., 1989. Azimuthal anisotropy in the earth from observations of SKS at GEOSCOPE and NARS broadband stations, *Bull. seism. Soc. Am.*, **79**, 1542–1558.

Vinnik, L. P., Kind, R., Kosarev, G. L. & Makeyeva, L. I., 1989. Azimuthal anisotropy in the lithosphere from observations of long-period  $S$ -waves, *Geophys. J. Int.*, **99**, 549–559.

## APPENDIX

### Conversion of $SH$ to $P$ at a dipping interface

Let us consider an incident  $S$ -wave on a dipping interface of normal vector  $\mathbf{n}$ . It is convenient to introduce a local coordinate system in the vicinity of the point of incidence. At the point of incidence, the polarization of the wave is given by

$$\mathbf{g}_S = U_1 \mathbf{e}_1 + U_2 \mathbf{e}_2 = \cos(g) \mathbf{e}_1 + \sin(g) \mathbf{e}_2$$

where  $\mathbf{e}_1$  and  $\mathbf{e}_2$  are two mutually perpendicular unit vectors both perpendicular to the ray. Vector  $\mathbf{e}_1$  lies in the plane of incidence, i.e. in the plane determined by the normal  $\mathbf{n}$  to the interface and the tangent  $\mathbf{t}$  to the ray at the point of incidence. Vector  $\mathbf{e}_2$  is perpendicular to this plane.  $g$  is the angle between vectors  $\mathbf{g}_S$  and  $\mathbf{e}_1$ . The transmitted  $P$ -wave is generated by the  $\mathbf{e}_1$  component of the incident  $S$ -wave and its amplitude is given by

$$U_P = C_S = C_{SV}(i) U_1 = C_{SV}(i) \cos(g),$$

where  $C_{SV}$  is the coefficient of transmission from  $SV$  to  $P$  corresponding to the angle of incidence  $i$ .

Let us assume for simplicity that the strike of the interface is parallel to the  $y$  axis. Then we can write the unit vector  $\mathbf{n} = \sin(f) \mathbf{e}_x + \cos(f) \mathbf{e}_z$ , where  $f$  is the dip of the interface. Moreover, we consider a plane  $SH$ -wave propagating in a direction parallel to the vertical plane  $x = 0$  containing the strike of the interface. The polarization of this  $SH$ -wave is then  $\mathbf{g}_S = \mathbf{e}_x$  and its direction of propagation is given by the unit vector  $\mathbf{t} = \cos(e) \mathbf{e}_y + \sin(e) \mathbf{e}_z$  where  $e$  is the emergence angle of the incident wave with respect to the horizontal plane. By definition of vector  $\mathbf{e}_2$ , we can write

$$\mathbf{e}_2 = \frac{\mathbf{t} \times \mathbf{n}}{\|\mathbf{t} \times \mathbf{n}\|}$$

where the cross product of two vectors has been denoted by  $\times$ .

It is not difficult to show that

$$\sin(g) = \mathbf{g}_S \cdot \mathbf{e}_2 = \frac{\cos(e)}{\sqrt{\cos^2(e) + \tan^2(f)}}$$

and

$$C_{SH} = C_{SV}(i) \frac{\tan(f)}{\sqrt{\cos^2(e) + \tan^2(f)}}.$$

Moreover, the incidence angle  $i$  is defined by

$$\cos(i) = \mathbf{t} \cdot \mathbf{n} = \cos(f) \sin(e).$$